Received 27 April 2020; revised 13 June 2020; accepted 16 June 2020. Date of publication 19 June 2020; date of current version 2 July 2020.

Digital Object Identifier 10.1109/OJAP.2020.3003718

Huygens Metasurface Lens for W-Band Switched Beam Antenna Applications

ANDREAS E. OLK [1,2] AND DAVID A. POWELL [1] (Senior Member, IEEE)

[1]School of Engineering and Information Technology, University of New South Wales, Canberra, ACT 2612, Australia

[2]Basics and Mathematical Modeling, IEE S.A., 7795 Luxembourg, Luxembourg

CORRESPONDING AUTHOR: A. E. OLK (e-mail: andreas.olk@iee.lu)

This work was supported in part by the Australian Research Council (Linkage Project) under Grant LP160100253, in part by the Luxembourg Ministry of the Economy under Grant CVN 18/17/RED, and in part by the University of New South Wales (UIPA Scholarship).

ABSTRACT Switched beam antennas provide an efficient and cost effective alternative to complex phased array and digital beam forming techniques. In this paper, we present the design and characterization of an electrically thin Huygens metasurface lens operating at 83 GHz with high transmission efficiency and we demonstrate its applicability to switched beam antenna applications. We accurately characterize the 3D scattered field distribution and determine the focal length and transmission efficiency of the lens by near-field scanning. A model based on ideal Huygens sources is used to predict the focal performance, allowing the geometrical measurement parameters to be determined in advance. Finally, the ability of the lens to operate as a switched beam antenna is experimentally verified by exciting it with an omnidirectional waveguide antenna placed at different positions. The experimental results are in very good agreement with numerical simulations, showing steering angles up to 12° while keeping the side lobe level below −15 dB.

INDEX TERMS Millimeter wave, flat lens, Huygens metasurface, switched beam antenna, near-field scanning, far-field antenna measurement.

I. INTRODUCTION

METASURFACES have been shown to enable versatile wavefront transformation, especially at microwave frequencies [1], [2]. They can enhance the directivity of antennas [3], [4], provide polarization control [5]–[8] and enable reconfigurability [9], [10]. Particular effort has been devoted to transforming the radiation of a compact non-directive source into directive radiation using passive metasurfaces [4], [11]–[15]. Accurate theoretical and numerical solutions to this problem using Huygens metasurfaces have been reported [12], [14]. By changing the lateral position of the source, the direction of the radiated wave can be controlled. Since in practice it is often implemented with multiple source antennas connected to the transmitter by RF switches, this configuration is referred to as a switched beam antenna.

The switched beam approach represents a promising alternative to more complex beam forming techniques. Low insertion losses can be achieved, and in contrast to phased array antennas [16], active phase shifting elements or additional delay lines are not required. This is particularly advantageous for high frequency systems, where the availability of efficient active components is reduced. Using this lens based antenna approach, highly directive radiation can be transmitted or received from different angles [17]–[21]. Several related configurations have been proposed in the literature, including steerable antennas based on ϵ-near-zero metamaterials [22], perforated dielectrics [23] and bent flexible metagratings [24].

Typical switched beam antennas utilise bulky dielectric or Fresnel lenses [25], [26], complicating the fabrication and integration of the antenna. Since Huygens metasurfaces are flat, and can be fabricated with printed circuit processes, their manufacturing and integration with other electronic components is much simpler [27]. Furthermore, Huygens metasurfaces can be designed to be impedance matched to free space, minimising the reflections back to the source.

For emerging microwave applications in telecommunications [28], [29] and radar [30], [31], frequencies in the millimeter wave (mm-wave) range are used, e.g., W-band

(75-110 GHz) and higher. In this part of the spectrum, the design and experimental characterization of highly transmissive metasurfaces is particular challenging [5], [6], [13]. For efficient Huygens type mm-wave metasurfaces consisting of three metallic layers, effects such as inter-layer near-field coupling [32], losses caused by conductor roughness [33], [34] and frequency shifts due fabrication tolerances are significant and have to be considered in the design.

Recently, we reported a novel synthesis method which incorporates near-field coupling and conductor roughness, minimizing such effects in an iterative optimization algorithm [32]. With this numerical method, highly efficient refracting mm-wave metasurfaces were experimentally demonstrated by extracting the intensity of Floquet harmonics from far-field measurements [33]. However, the design and experimental characterization of a non-periodic metasurface lens requires detailed near-field measurements [15], [35], [36]. Because of these challenges, experimental demonstrations of efficient metasurface lenses operating at W-band or higher frequencies have been scarcely reported. Thus it has not been demonstrated whether their performance is sufficient to enable a switched beam antenna.

In this paper, we design and characterize a flat Huygens metasurface lens operating at 83 GHz with high transmission efficiency, and we investigate its applicability to switched beam antennas. We use the standard hyperbolic phase profile to design the metasurface lens, and the synthesis procedure minimizes performance degradation due to interlayer near-field coupling and copper roughness, which are particularly problematic at W-band. Using near-field scanning, we overcome previous limitations in the experimental characterization and determine the focal length as well as the transmission efficiency precisely. An efficient semi-analytical model based on ideal Huygens sources enables modelling of the complete lens aperture. This model is used to create reference data and it allows the measurement region to be determined in advance. Furthermore, we demonstrate the switched beam functionality using a single commercial omnidirectional waveguide antenna to excite the metasurface from different positions. The far-field radiation pattern is measured with high resolution using a bistatic facility located in an anechoic chamber and the experimental results are in very good agreement with our semi-analytical model.

II. DESIGN AND FABRICATION OF FLAT HUYGENS METASURFACE LENS

We design a metasurface lens with near unity transmission amplitude and a hyperbolic transmission phase profile ϕ_{des} [15] along the x direction

$$\phi_{des}(x) = \frac{2\pi}{\lambda}\left(\sqrt{x^2 + f_{focal}^2} - f_{focal}\right) + \phi_0. \qquad (1)$$

Here, λ is the operating wavelength and f_{focal} is the focal length. Such a lens can be used to collimate antenna radiation in the x direction while maintaining its beam width in the y direction. We use a focal length of $f_{focal} = 27.4\,\text{mm} \approx 7.6\lambda$.

We aim to achieve a high transmission efficiency at the center frequency and we want to maintain compatibility with commercial printed circuit board (PCB) processes. Therefore, we utilize a Huygens metasurface architecture with three metallic layers spaced by dielectrics, similar to previous work [32], [33], [37]. The dielectric substrate Isola Astra MT has a relative permittivity of 3.0 and a loss tangent of 0.0017 and it allows us to space the metallic layers by 254 µm. Each layer contains resonators in the shape of a dogbone as shown in Figure 1 (a) and the geometrical parameters G_n and S_n are varied to control the sheet impedance of each layer. The height of the unit cell $a_y = \lambda/3.5$ is fixed by the dogbone structure, whereas the width $a_x = \lambda/2.5$ is chosen as a balance between good discretisation of the surface impedance, and avoiding strong interaction between neighbouring cells. At W-band frequencies, this coarse discretization and the comparably large resonating elements are necessary to reach high efficiency and an accurate transmission phase despite the limited resolution of the photolithography in PCB manufacturing. For the same reason, metallic shapes are designed with an edge radius of $> 30\,\mu$m. More detailed information on this high frequency meta-atom design are found in [33].

This design is suited to linear polarization with electric field oriented along the y-direction, as we use throughout this work. In the case of Huygens metasurfaces, the required sheet impedance of the outer layers is identical, therefore we stipulate $G_1 = G_3$ and $S_1 = S_3$. Other geometrical dimensions are $W = 0.6\,\text{mm}$, $H = 0.1\,\text{mm}$, $R_{cv} = 30\,\mu\text{m}$ and $R_{cc} = 40\,\mu\text{m}$. The thickness of the metallic layers is 18 µm. The rectangular cell geometry is beneficial for the symmetry of the lens (mirror symmetric about the y axis, repetition of cells in y direction). This allows modelling of the lens by simulating only a single row of cells along the x direction, as shown in Section IV.

As shown on the microscopy photo in Figure 1 (b), the aperture size of the lens is $d_x \times d_y = 33\,\text{mm} \times 32\,\text{mm}$, which corresponds to 22×30 cells or $\sim 9 \times 9$ wavelengths. Outside of this rectangular area, a closed metallic surface is applied to the outer layers during the PCB fabrication. This creates a well defined aperture edge for the experiment, although it may lead to some reflections back to the source. The size of the lens aperture was chosen to give a good compromise between performance and practicality in the experiment. With a larger aperture, a smaller focal spot could be achieved, however the characterization by near-field scanning would take longer (more details in Section III). The geometrical parameters $G_{1,2}$ and $S_{1,2}$ of each cell are determined following the iterative synthesis method from [32]. With this method, secondary effects that can cause performance degradation, such as inter-layer near-field coupling and losses induced by copper roughness, are minimized [33].

Due to the symmetry of the design, only 11 different cells are required. We label these cells with an index l. We note that the lens was initially designed for operating at

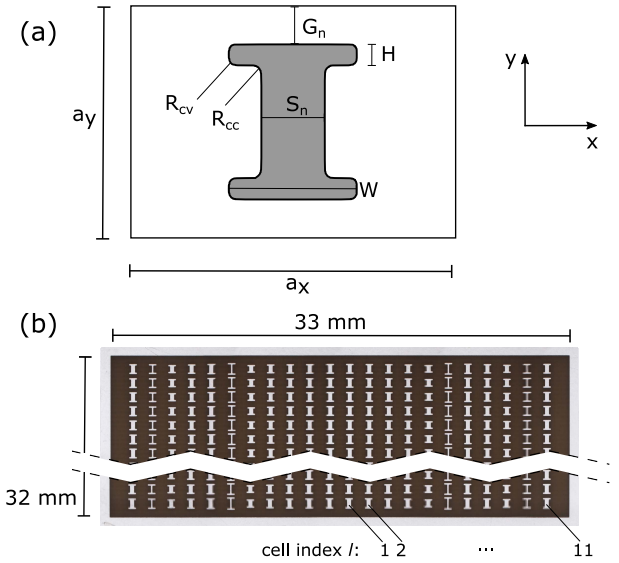

FIGURE 1. (a) Unit cell layout. Grey color indicates metallic parts. (b) Flat lens sample with metallic aperture.

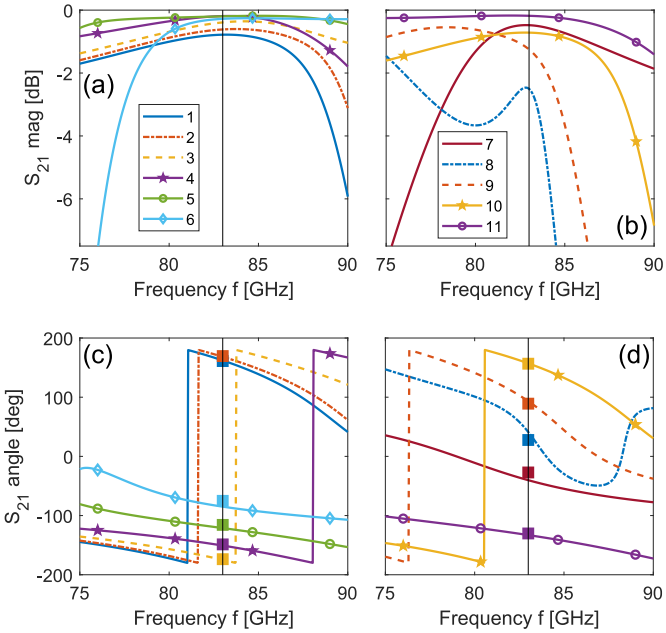

FIGURE 2. Simulated transmission S_{21} of the individual cells. Amplitude (a), (b) and phase (c), (d). Cells with index 1 to 6 (a), (c) and index 7-11 (b), (d).

80 GHz, however fabrication tolerance shifted the frequency of optimal performance to 83 GHz. The lens was manufactured in the same batch as the structures previously reported in [33], which includes a detailed analysis of the fabrication tolerances.

In Figure 2, the transmission properties of each cell are shown, determined from full-wave simulation with *CST Microwave Studio* [38], incorporating the measured changes to the fabricated geometry. The frequency of optimal performance is indicated by a black vertical line and the desired transmission phase ϕ_{des} is indicated with solid squares. Due to the use of the iterative design method, the desired transmission phase is achieved relatively accurately. The transmission amplitude $|S_{21}|^2$ of most cells is 84 % (−0.8 dB) or higher, except for cells 8 and 9, cells which have a transmission phase near zero. Many early works on Huygens metasurfaces in the microwave frequency range show full 2π phase coverage with near unity transmission amplitude using structures with out of plane metallic elements [39]–[41]. For more practical planar three layer structures, it is known that a full 2π phase coverage is difficult to achieve with a single resonator architecture. In [42], this effect was investigated using coupled mode theory and the authors suggest to combine a three layer structure with two layer cells for small transmission phase values. This result is in agreement with other works, where different resonator shapes have been combined to meet the sheet impedance requirements [41], [43].

We note that bandwidth of the lens could be further improved through fitting the impedance and its frequency derivative to an LC circuit, similar to what was shown for a reflective structure in [43]. The transmission efficiency of each cell could be further improved by introducing Omega-bianisotropy, leading to non-identical outer layers [37], [44]. However, the efficiency gain is not significant for scattering angles below 55°, and our structure has a maximum scattering angle of 37°. In this work, we have chosen the free phase offset $\phi_0 = -200°$ to maximise the transmission amplitude, however no further numerical optimization was applied to adjust the shape of resonators. We note that the simulated transmission phase and the desired phase of the cells agree very well, and the simulated average value of the transmitted power is 86 %. The cross-polarized scattered field is very low, being at least 40 dB below the co-polarized field in the full-wave simulation.

III. FOCUSING PERFORMANCE

In this section, the transmission efficiency as well as the focal length of the lens are validated experimentally by means of near-field scanning. We note that for metasurfaces where the focusing behaviour is not well approximated by geometric optics, it is important to discriminate between the point of maximum amplitude, and the point where all waves converge in phase [15]. In the literature, the response of metasurface lenses is often characterized with an amplitude measurement [45], [46]. This method is simple, as it does not require a coherent detector, and it can be measured with a relatively low scan resolution.

However, due to the $1/r$ contribution of the scattered field from each cell, the amplitude maximum is typically closer to the metasurface than the true phase focus [15]. Therefore, in the experiment, we measure the phase focal point, which is expected to correspond best to the designed focal length f_{focal} in Eq. (1), and is the correct location for a feed in lens antenna applications.

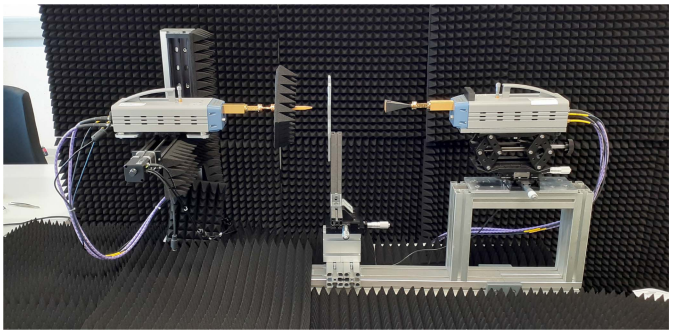

FIGURE 3. Near-field scanning setup with standard horn antenna exciting the mm-wave lens.

When exciting a lens with a plane wave, the phase focal point (or phase center) occurs at a distance of the focal length f_{focal}. In the experiment, plane wave excitation is approximated with a standard gain (25 dB) horn antenna illuminating the lens from the far-field. Therefore, we first measure the impinging wavefront with the metasurface removed. This information is then used to simulate and measure the field scattered from the lens, in order to verify that the design focal length was accurately realized. Finally, we evaluate the frequency dependent performance criteria, such as the overall transmission efficiency and the peak intensity in the focal plane from experimental data.

The experimental near-field scanning setup is shown in Figure 3. Two motorized linear stages support the near-field probe and they can be mounted for scanning in the xy or the xz plane. The transmitting antenna and the sample holder that carries the metasurfaces lens are mounted on a rail, enabling their separation to be adjusted with a precision of <1 mm. Alignment lasers help to keep all components on the same height and well adjusted with respect to the optical axis z. We use a vector network analyzer (VNA) with external mixers (*Rohde & Schwarz ZVA110*) and we perform a TOSM calibration (through offset-short match) with WR10 waveguide standards to set the reference planes to the feeding side of the horn antenna (*Mi-Wave 261W/387*) and the near-field probe (*Vivatech VTWGP-10*), respectively.

A. IMPINGING WAVEFRONT

In Figure 4 (a), the measurement configuration for characterizing the impinging wavefront is shown. The scanning plane $z_m = 0$ is located at a distance of 200 mm from the aperture of the horn antenna. In Figure 4 (b) and (c) we show the measured amplitude and the phase distribution at 83 GHz. The solid black rectangle indicates the position of the lens aperture for the subsequent lens measurements (the sample was removed for the measurement shown in this subsection). As we observe a rather smooth variation of phase and amplitude, we used a coarse step width of 4 mm $\approx\lambda$ for the scan. In Figure 4 (d) and (e), cross sections through this data at $y = 0$ are shown. We observe that the amplitude and phase distributions are similar to a Gaussian beam. Therefore, we fit a Gaussian intensity and a parabolic phase

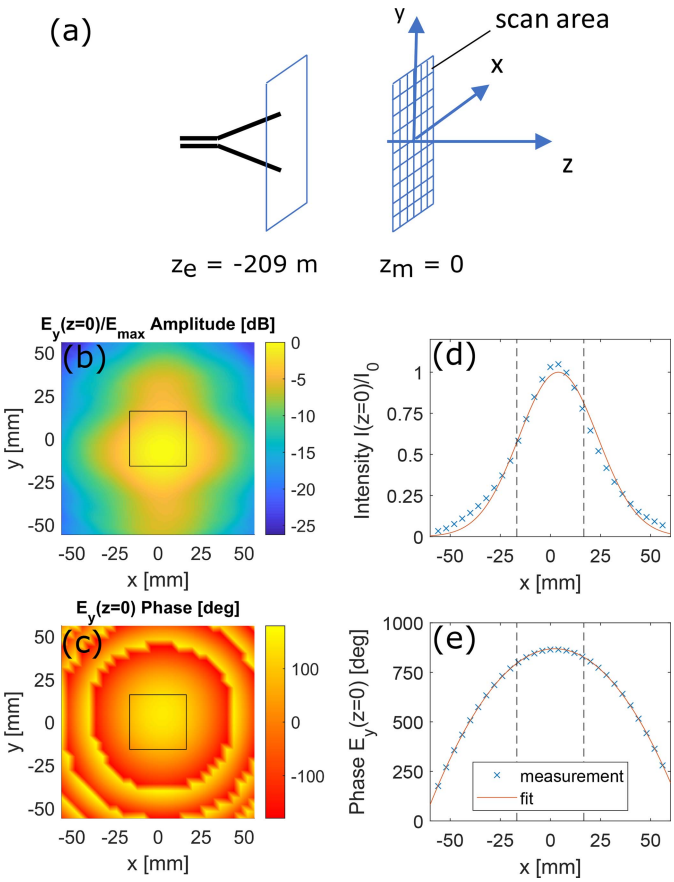

FIGURE 4. (a) Measurement configuration for the characterization of the impinging wavefront and results for (b) amplitude and (c) phase. Gaussian beam fit to a $y = 0$ cross section of the measurement data, (d) amplitude and (e) phase. Vertical dashed lines indicate the size of the lens aperture.

profile, and we use this fitted data in the following. Due to this phase profile, near the optical axis, the impinging wavefront can be approximated as a point source originating from $z_e = -209$ mm which can be used for geometric optics estimations.

B. FOCAL LENGTH

As we excite the lens with a non-planar phase front, the focal point z_{fp} will be observed at a distance greater then the actual focal length f_{focal}. This distance can be estimated with the Newtonian image equation

$$\frac{1}{f_{focal}} = \frac{1}{|z_e|} + \frac{1}{z_{fp}}. \tag{2}$$

This yields $z_{fp} = 31.5$ mm. In addition to this geometrical estimate, we calculate the electric field scattered from the lens aperture to determine the phase focal point precisely.

Simulating the scattered field with full-wave simulation can be time consuming, since the metasurface contains many fine details, and the required simulation domain is relatively large. Therefore, we model the metasurface lens with an array of ideal Huygens sources (collocated ideal electric and magnetic dipoles), as shown in Figure 5 (a). The electric

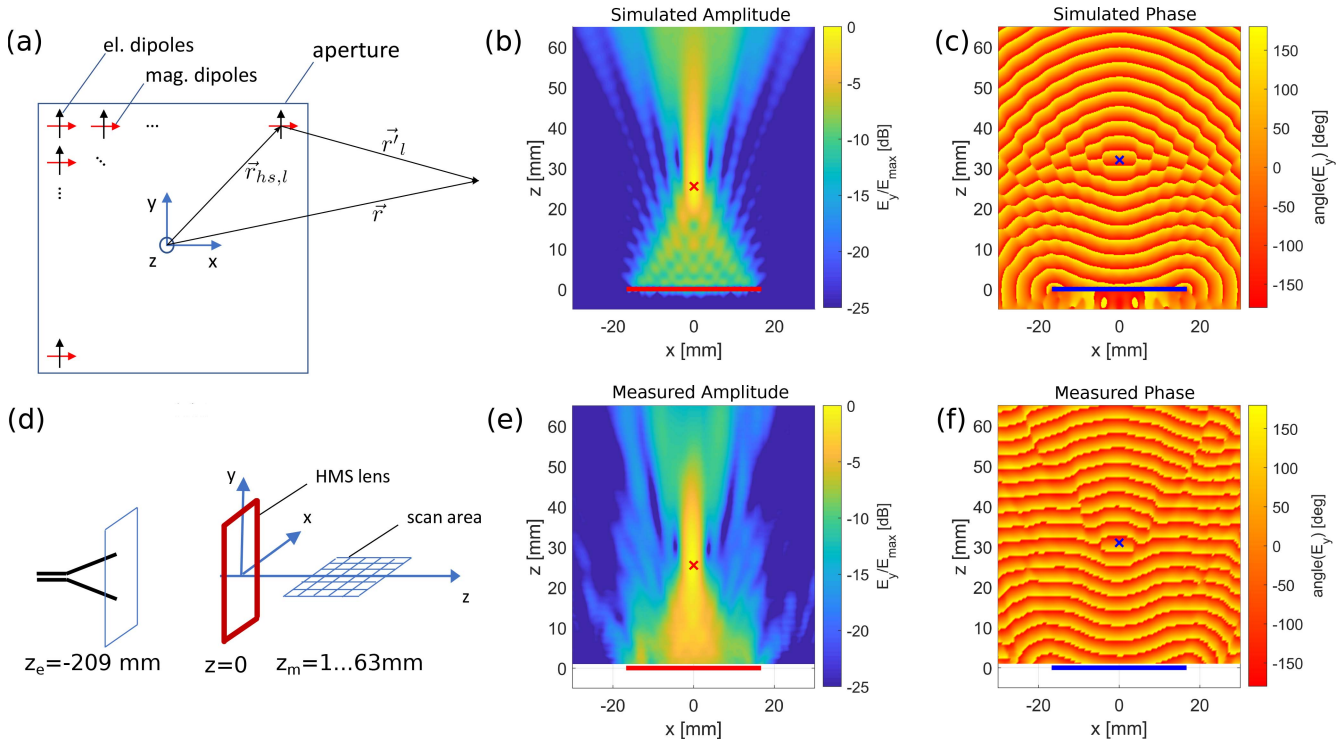

FIGURE 5. (a) Simulation configuration for the determination of the phase center. (b-c) Simulated field E_y in the $y = 0$ plane. (d) Measurement configuration and (e-f) measured field E_y in the $y = 0$ plane. In (b-c) and (e-f), the position of the lens at $z = 0$ is indicated by a thick solid line. Additionally, the amplitude maximum (b, e) and phase focal point (c, f) is indicated by a red and blue cross marker, respectively.

dipoles $\vec{p}$ are oriented parallel to the y-axis and the magnetic dipoles $\vec{m}$ are oriented parallel to the x-axis. In particular, for a Huygens source l at position $\vec{r}_{hs,l}$, we use dipole moments of the form

$$\vec{p}_l = p_0\, e^{i\phi_{des}(x_l)}\, \frac{E_y(x_l, y_l, z=0)}{E_{max}}\, \hat{e}_y, \tag{3}$$

$$\vec{m}_l = m_0\, e^{i\phi_{des}(x_l)}\, \frac{E_y(x_l, y_l, z=0)}{E_{max}}\, \hat{e}_x. \tag{4}$$

Here, $e^{i\phi_{des}(x_l)}$ is a complex scalar weight which represents the transmission properties of the lens. Similarly, the electric field ratio E_y/E_{max} is a weight that represents the impinging wavefront and is determined from the fitted data in Figure 4. The ratio of the unweighted dipole moments p_0 and m_0 is chosen such that electric and magnetic dipoles radiate the same amount of power, i.e., $m_0 = c\, p_0$ with the speed of light c. As we are mainly interested in the phase and the relative amplitude distribution, the overall power that is radiated from each Huygens source is chosen arbitrarily as

$$P_{tot} = 2P_{el} = 2\frac{c_0^2\eta}{12\pi}k^4 p_0^2 = 1\,\mathrm{W} \tag{5}$$

with η indicating the free space impedance and k the wavenumber $2\pi/\lambda$. Finally, we determine the total electric field scattered from the array as

$$\vec{E}_{total}(\vec{r}) = \sum_l \left(\vec{E}_p\left(\vec{r}'_l\right) + \vec{E}_m\left(\vec{r}'_l\right)\right). \tag{6}$$

Here, $\vec{r}'_l = \vec{r} - \vec{r}_{hs,l}$ as in Figure 5 (a), the sum includes all dipoles l within the aperture and $\vec{E}_{p/m}$ indicates the field scattered from a single electric/magnetic dipole. The corresponding expressions for $\vec{E}_{p,m}$ are given by Eqs. (10) and (11) in the Appendix. Finally, Equation (6) was evaluated numerically (*MATLAB*). Note that in Eqs. (3) and (4) we assume full transmission for all of the cells, and include only the phase factor $e^{i\phi_{des}}$. This means that our model represents the scattering from an ideal lens, serving as a benchmark for our experimental results, to show the effect of all design and experimental imperfections.

In Figure 5 (b) and (c), the simulated amplitude and phase distribution of the scattered electric field E_y are shown. The position of the lens at $z = 0$ is indicated by a thick solid line. The plotted field amplitude is normalized by the maximum value E_{max}. A significant field enhancement in front of the metasurface is clearly discernible and the amplitude maximum occurs at $z = 25.5\,\mathrm{mm}$. In the phase distribution, a change of curvature of the phase front occurs at $z = 31.5\,\mathrm{mm}$ which is in agreement with Eq. (2). This phase center is indicated with a blue cross marker in Figure 5 (c). The experimental configuration for the determination of the phase center is shown in Figure 5 (d). Here, the metasurface lens is placed in the plane where the incident field was measured (Figure 4). In order to resolve the phase distribution accurately, we use a step width of $0.5\,\mathrm{mm}=\lambda/7.5$. The measurement plane is in the xz-plane and the size of the scan is $64\,\mathrm{mm} \times 64\,\mathrm{mm}$. We started the scan as close as

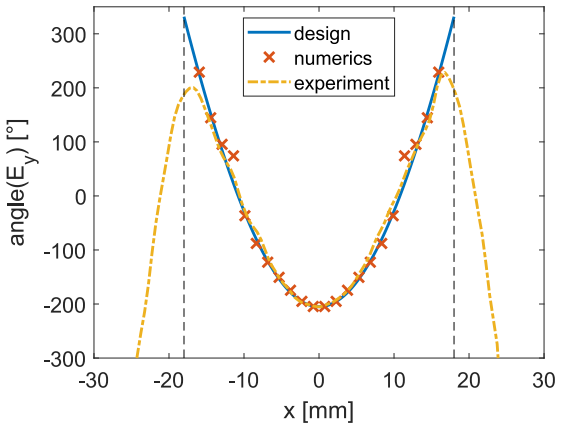

FIGURE 6. Comparison of the designed transmission phase ϕ_{des} with the measured phase $\angle E_y$ close to the flat lens, i.e., $z = 1$ mm. The red cross markers indicate the result obtained from full-wave simulations of the individual cells.

1 mm to the lens, and the total measurement duration was approximately 22 h.

The measurement results are shown in Figure 5 (e) and (f). Good agreement is observed between the measured and simulated amplitude distributions. The measured amplitude maximum occurs at $z = 25.5$ mm, which coincides with the simulation. In the simulated amplitude distribution, Figure 5 (b), an interference pattern occurs close to the metasurface, due to the simulation being based on ideal point dipoles. In the measurement, these interference patterns are smeared out due to the non-negligible size of the resonators and the measurement probe. The phase distribution in Figure 5 (e) is in very good agreement with the simulation result. Significant differences occur only on the sides of the measurement area where the amplitude is very low. The measured phase center occurs at $z = 31$ mm. The discrepancy between simulated and measured phase center is roughly 2 %. This result indicates that the design focal length f_{focal} was realized with a similar precision.

We directly compare the designed and realized phase distribution in Figure 6. Here, the designed transmission phase $\phi_{des}(x)$ (blue solid line) and the measured phase of the field close to the metasurface $\angle E_y$ at $z = 1$ mm are shown. Additionally, we show the transmission phase as obtained from the full-wave simulation of individual cells at 83 GHz with crosses. This representation of the transmission phase is meaningful for an analysis of defects of individual cells. Here, good overall agreement between design, numerics and experiment is observed. This confirms that the design data from Figure 2 was realized accurately. It is also discernible that the influence of the phase mismatch of cell number 8 on the overall phase distribution of the transmitted field is relatively small.

C. TRANSVERSE PROFILE OF FOCUSED BEAM

To analyze the shape of the focused beam, we record a near-field scan in the plane of the phase center $z_m = 31$ mm. The measurement configuration is shown in Figure 7 (a). To find

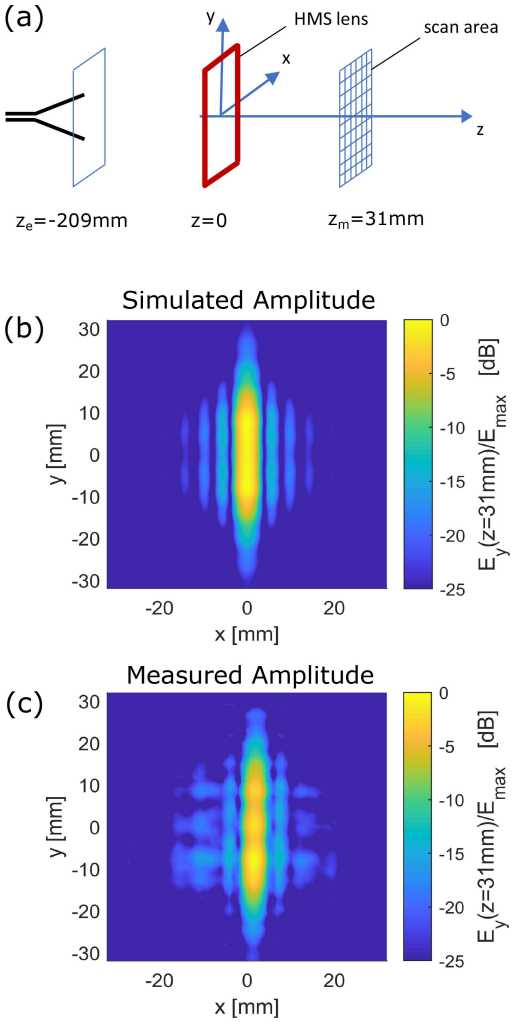

FIGURE 7. Configuration for measuring the electric field in the plane of the phase center $z = 31$ mm (a). Result of simulation (b) and experiment (c) in comparison.

the optimal scanning area, the dipole model is used to predict the focused beam shape. We simulate the scattered field using Equation (6) similar to Section III-B. The simulation result is shown in Figure 7 (b). As expected for focusing along a single axis, most of the energy is focused onto a line at $x = 0$. Along the y-direction and within the aperture, i.e., $|y| \geq 16$ mm, the amplitude is almost constant. The simulation confirms that the amplitude at the boundaries of the scanned region is mostly decayed to values -25 dB lower than the maximum E_{max}.

In order to remove artifacts such as undesired reflections within the experimental setup, we apply time domain gating. The gating function is a Hann window ranging from 0.2 to 2.3 ns corresponding to a length of 5 to 70 cm. This gating is particularly important for a frequency dependent analysis. The measured amplitude in the focal plane after time-gating is shown in Figure 7 (c). The overall amplitude distribution is in good agreement with the simulation. We compare the power incident on the aperture P_{inc} at $z = 0$ with the power P_{pc} measured in the plane of the phase center $z = z_{pc}$ and

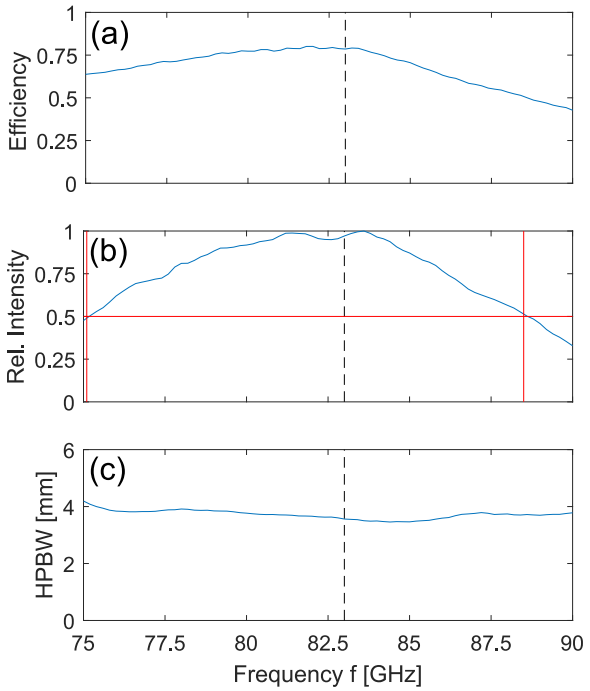

FIGURE 8. Variation with frequency of (a) efficiency, (b) peak intensity and (c) beam width of the focal spot. The dashed black line indicates the optimal operating frequency 83 GHz.

evaluate the transmission efficiency P_{pc}/P_{inc}. In particular, P_{pc} is determined by integrating the measured field over the full scan area $l_x \times l_y$ shown in Figure 7 (c) and can be written as

$$P_{pc} = \int_{-l_y/2}^{+l_y/2} \int_{-l_x/2}^{+l_x/2} \left|E_y\left(z = z_{pc}\right)\right|^2 dxdy. \tag{7}$$

Similarly, the incident power P_{inc} is determined with data from Section III-A and can be written as

$$P_{inc} = \int_{-d_y/2}^{+d_y/2} \int_{-d_x/2}^{+d_x/2} \left|E_y(z = 0)\right|^2 dxdy. \tag{8}$$

Here, the integration area $d_x \times d_y$ corresponds to the aperture as indicated by the black rectangle in Figure 4 (b). In Figure 8 (a), the transmission efficiency P_{pc}/P_{inc} is plotted versus frequency. The maximum efficiency of 76 % is found at 83 GHz. Due to non-idealities such as scattering from the aperture edge or higher diffraction orders which radiate outside the scanned area, this value is smaller than the mean transmission of 86 % obtained from the individual cell simulations shown in Section II. This result is in good agreement with [3], where the overall transmission efficiency of a Huygens metasurface lens operating at lower frequencies was estimated by integrating the main lobe of the far-field pattern. Therefore, the method used here represents an intuitive and practical alternative in cases where near-field information is available.

Additionally, we evaluate the maximum intensity as a function of frequency. There are significant variations along y, therefore the overall maximum of $|E_y|^2$ is not a very stable quantity. We choose here to evaluate the peak intensity for constant $y = y'$ within a range of $|y| \geq \delta_y/2 = 10\,\text{mm}$ and determine the average over these peak values, i.e.,

$$\frac{1}{\delta_y} \int_{-\delta_y/2}^{\delta_y/2} \max_x \left(\left|E_y(x, y')\right|^2\right) dy'. \tag{9}$$

The result is shown in Figure 8 (b). Also in this case, we see optimal performance at 83 GHz and we observe that the relative intensity is above 0.5 within a frequency range of more than 10 GHz, marked by the red lines in Figure 8 (b). As a third performance metric, the half power beam width (HPBW) is determined. Again, we determine the HPBW in the x-direction for all values of y' with $|y| \geq \delta_y/2$ and determine the average. As shown in Figure 8 (c), the beam width is fairly constant with frequency within the measured range. This indicates that the reduction in intensity away from the optimal frequency is not due to degradation of the beam shape, rather it comes from the reduced transmission of individual cells shown in Fig. 2.

IV. SWITCHED BEAM ANTENNA FUNCTIONALITY

Having verified the focal length and the transmission efficiency of the lens, we excite it with a non-directional source to create directive radiation. First, this configuration is analyzed in full-wave simulation (*CST MWS* [38]) using a wire dipole as the excitation source. To reduce the computational effort, we model one row of cells of height a_y, with perfect electrical conductor upper boundaries. For this row of cells, we consider the full three layer geometry. The lens is excited with a feed dipole placed at a distance of $f_{focal} = 27.4\,\text{mm}$. The resulting field distribution is shown in Figure 9. By varying the lateral displacement of the feed dipole Δx, the direction of radiation from the aperture can be varied. We use this simulated field at $z = 10\,\text{mm}$ in a near-field to far-field transformation [47], [48]. The result is shown in Figure 11 and is discussed later in this subsection.

In the experiment, a commercial omnidirectional waveguide antenna (*Mi-Wave 267W-92/387*) is used for excitation. The measurement configuration is shown in Figure 10 (a). This antenna is fed from an external frequency extender of the VNA. Therefore, as shown in Figure 10 (b), the overall transmitting unit consists of several components that are rigidly connected, i.e., frequency extender, omnidirectional source and lens with sample holder. Since these components need to be precisely aligned with each other, they are mounted on optical translation stages. As this overall transmitting unit is rather bulky, it remains static during the measurement and the receiving unit of a bistatic setup moves around it on a circle with 1 m radius. To reduce measurement artifacts caused by undesired reflections, all far-field measurements are performed in an anechoic chamber. More details to the bistatic system can be found in [49].

The normalized directivity D/D_{max} values obtained from experiment and simulation are compared in Figure 11. Here, D_{max} indicates the maximum directivity, $D_{max} = D(\theta = 0, \Delta x = 0)$, and this single value of D_{max} is used

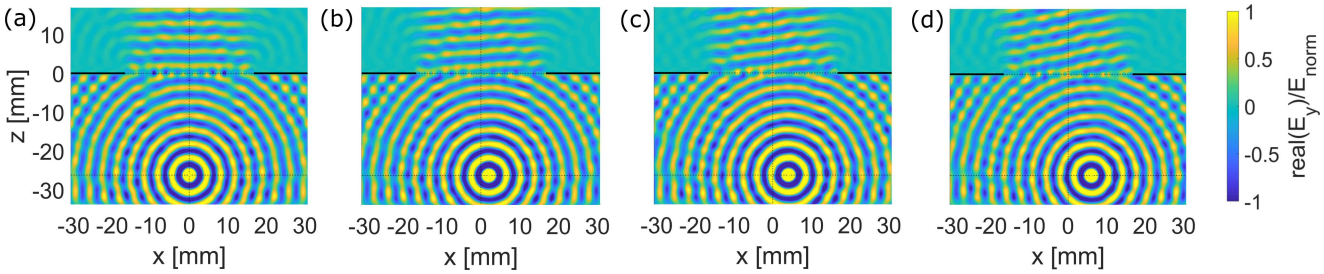

FIGURE 9. Excitation of the flat HMS lens with electric dipole. Simulated field E_y in $y = 0$ plane for different lateral displacements of the dipole source.

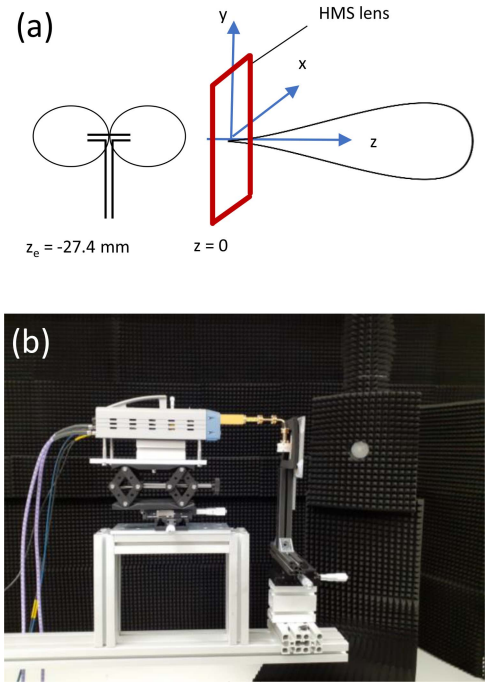

FIGURE 10. Measurement configuration for the far-field characterization of the switched beam antenna (a) and experimental setup (b).

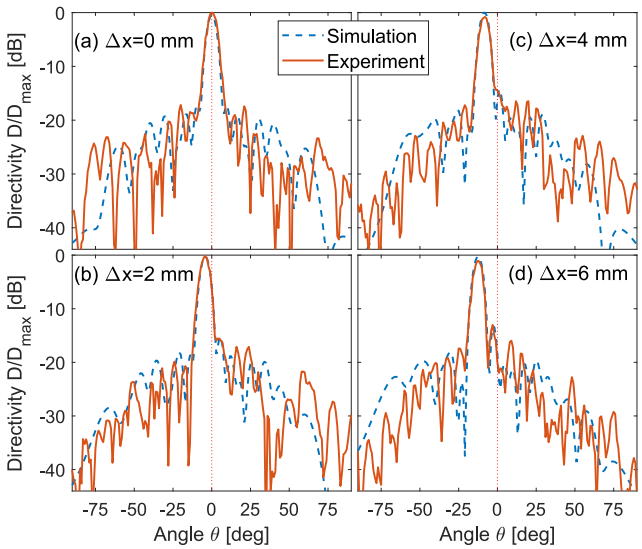

FIGURE 11. Comparison of the simulated and measured far-field pattern, showing beam steering when varying the position of the feed antenna Δx.

to normalize all four subfigures. Due to the lack of a reference antenna with precisely specified gain, we are unable to calibrate the bistatic measurement system to determine the absolute gain of the antenna system. The directivity is shown with variation of the angle θ for $\phi = 90°$, i.e., the cutting plane is the xz-plane. Good agreement is achieved, particularly about the main lobe. The half power beam width is roughly 6.5 ° in all configurations shown. By increasing the lateral offset Δx to 6 mm, the main radiation direction reduces linearly to $\theta = -12°$. The side lobe level of the presented antenna system is fairly low. For Δx up to 4 mm, it is significantly lower than -15 dB. For $\Delta x = 6$ mm, one side lobe at $\theta = -3°$ slightly exceeds -15 dB and it increases for larger values of Δx, as typically observed in steerable antennas [50]. The overlap of the half power main lobes of these different configurations is on the order of 2°.

Within the range shown in Figure 11, the reduction of the directivity for increasing θ (scan-loss) was observed to be relatively small with <0.5 dB in the simulation and <1.1 dB in the experiment. Therefore, the usable scanning range is mainly limited by the occurrence of side-lobes. For the other cutting plane, $\phi = 0$, a half power beam width of 38° and a side lobe level of -15.3 dB was measured. Far-field measurements of the cross-polarized electric field show a maximum normalized directivity <-34 dB in all four cases of Δx. Due to the symmetry of the system, these results (Fig. 11) show that by exiting the lens from seven equidistant positions $x = (-6, -4, \ldots, +6)$ mm, a switched beam antenna with scan range of $\theta = -12 \cdots 12°$ can be realized. Such antenna properties are required for instance in mm-wave radar sensing.

The bandwidth of the proposed antenna system depends mainly on three aspects. First, it is limited by the transmittance of the lens. In Section III-C, we showed that the relative field intensity near the focal point is above 0.5 in a range from 75.2 to 88.3 GHz. Secondly, the main lobe maximum is sensitive to small variations of the phase focal point which can further limit the bandwidth of the overall system. Full-wave simulations with an ideal wire dipole as excitation source (as in Figure 9) show that this reduces the operation bandwidth further to 78.0 to 88.0 GHz. The third limitation is the bandwidth of the excitation source.

Due to the fact that the omnidirectional waveguide antenna represents a generic source for demonstration purposes and also due to the calibration issues mentioned above, we did not investigate the bandwidth of this excitation source. The frequency ranges above indicate that using a suitable source, a bandwidth of several GHz could be reached.

The presented experiment with the omnidirectional waveguide antenna proves the viability of this metasurface lens as a switched beam antenna, and gives an estimate of the system performance. However, this excitation source is too bulky for most mm-wave applications such as 5G communication or radar sensing. In this context, planar circuit board antennas are commonly used. Therefore, for future studies, an excitation of the lens with multiple microstrip patch antennas is envisaged. This would require an additional optimization step to adapt the lens to radiation characteristics which are significantly different to the dipole radiation. Additionally, in this work, the focal length of the lens was chosen as the minimum distance required due to the size of the waveguide antenna. Notably, the gap between the outer edge of the waveguide and the lens was on the order of 3 mm (Figure 10 (b)). With revised planar excitation sources, designs with smaller focal length and greatly improved compactness are possible.

V. CONCLUSION

We presented the design and the characterization of a Huygens metasurface lens operating at 83 GHz with high transmission and demonstrated its applicability as integral part of a switched beam antenna. By comparing the energy of the incident wave and the energy in the plane of the phase center, we rigorously evaluate the transmission efficiency of the lens. A simplified model based on ideal Huygens sources was used to create reference data, allowing the geometrical parameters of the measurement to be determined in advance. With the help of this model, the focal length of the lens was verified experimentally to a high precision. Switched beam functionality was demonstrated using an omnidirectional waveguide antenna for excitation of the metasurface. The side lobe level of the system is on the order of -15 dB and the experimental results are in very good agreement with numerical simulations.

APPENDIX

The scattered electric field of an electric dipole $\vec{p}$ is written as [51]:

$$\vec{E}_p(\vec{r}) = \frac{1}{4\pi\epsilon_0}\left\{k^2(\vec{n}\times\vec{p})\times\vec{n}\,\frac{e^{ikr}}{r} + \left[3\vec{n}(\vec{n}\cdot\vec{p})-\vec{p}\right]\left(\frac{1}{r^3}-\frac{ik}{r^2}\right)\right\}. \quad (10)$$

Here, r is the absolute value of $\vec{r}$ and $\vec{n}$ indicates the unit vector parallel to $\vec{r}$, i.e., $\vec{n} = \vec{r}/r$. The scattered electric field of a magnetic dipole $\vec{m}$ [51] is written as:

$$\vec{E}_m(\vec{r}) = -\frac{\eta}{4\pi}k^2(\vec{n}\times\vec{m})\frac{e^{ikr}}{r}\left(1-\frac{1}{ikr}\right). \quad (11)$$

REFERENCES

[1] F. Ding, A. Pors, and S. I. Bozhevolnyi, "Gradient metasurfaces: A review of fundamentals and applications," *Rep. Progr. Phys.*, vol. 81, no. 2, Feb. 2018, Art. no. 026401.

[2] S. B. Glybovski, S. A. Tretyakov, P. A. Belov, Y. S. Kivshar, and C. R. Simovski, "Metasurfaces: From microwaves to visible," *Phys. Rep.*, vol. 634, pp. 1–72, May 2016.

[3] M. Chen, A. Epstein, and G. V. Eleftheriades, "Design and experimental verification of a passive Huygens' metasurface lens for gain enhancement of frequency-scanning slotted-waveguide antennas," *IEEE Trans. Antennas Propag.*, vol. 67, no. 7, pp. 4678–4692, Jul. 2019.

[4] J. Han, L. Li, T. Zhang, and R. Xi, "Control and improvement of antenna gain by using multilayer non-uniform metasurfaces," *EPJ Appl. Metamater.*, vol. 6, p. 4, Jan. 2019.

[5] C. Pfeiffer and A. Grbic, "Millimeter-wave transmitarrays for wavefront and polarization control," *IEEE Trans. Microw. Theory Techn.*, vol. 61, no. 12, pp. 4407–4417, Dec. 2013.

[6] C. Pfeiffer and A. Grbic, "Bianisotropic metasurfaces for optimal polarization control: Analysis and synthesis," *Phys. Rev. Appl.*, vol. 2, no. 4, Oct. 2014, Art. no. 044011.

[7] Y. Yuan, K. Zhang, X. Ding, B. Ratni, S. N. Burokur, and Q. Wu, "Complementary transmissive ultra-thin meta-deflectors for broadband polarization-independent refractions in the microwave region," *Photon. Res.*, vol. 7, no. 1, pp. 80–88, Jan. 2019.

[8] K. Zhang, Y. Yuan, X. Ding, B. Ratni, S. N. Burokur, and Q. Wu, "High-efficiency metalenses with switchable functionalities in microwave region," *ACS Appl. Mater. Interfaces*, vol. 11, no. 31, pp. 28423–28430, Aug. 2019.

[9] M. Liu, D. A. Powell, Y. Zarate, and I. V. Shadrivov, "Huygens' metadevices for parametric waves," *Phys. Rev. X*, vol. 8, no. 3, Sep. 2018, Art. no. 031077.

[10] H. Yang *et al.*, "A programmable metasurface with dynamic polarization, scattering and focusing control," *Sci. Rep.*, vol. 6, Oct. 2016, Art. no. 35692.

[11] C. Xue, Q. Lou, and Z. N. Chen, "Broadband double-layered Huygens' metasurface lens antenna for 5G millimeter-wave systems," *IEEE Trans. Antennas Propag.*, vol. 68, no. 3, pp. 1468–1476, Mar. 2020.

[12] A. Epstein and G. V. Eleftheriades, "Passive lossless Huygens metasurfaces for conversion of arbitrary source field to directive radiation," *IEEE Trans. Antennas Propag.*, vol. 62, no. 11, pp. 5680–5695, Nov. 2014.

[13] D. Kitayama, M. Yaita, and H.-J. Song, "Laminated metamaterial flat lens at millimeter-wave frequencies," *Opt. Exp.*, vol. 23, no. 18, pp. 23348–23356, Sep. 2015.

[14] A. Epstein and G. V. Eleftheriades, "Huygens' metasurfaces via the equivalence principle: Design and applications," *J. Opt. Soc. Amer. B*, vol. 33, no. 2, pp. A31–A50, 2016.

[15] C. Saeidi and D. van der Weide, "A figure of merit for focusing metasurfaces," *Appl. Phys. Lett.*, vol. 106, no. 11, Mar. 2015, Art. no. 113110.

[16] J. S. Herd and M. D. Conway, "The evolution to modern phased array architectures," *Proc. IEEE*, vol. 104, no. 3, pp. 519–529, Mar. 2016.

[17] Y. J. Cho, G.-Y. Suk, B. Kim, D. K. Kim, and C.-B. Chae, "RF lens-embedded antenna array for mmWave MIMO: Design and performance," *IEEE Commun. Mag.*, vol. 56, no. 7, pp. 42–48, Jul. 2018.

[18] Y. Zeng and R. Zhang, "Millimeter wave MIMO with lens antenna array: A new path division multiplexing paradigm," *IEEE Trans. Commun.*, vol. 64, no. 4, pp. 1557–1571, Apr. 2016.

[19] T. Xie, L. Dai, X. Gao, H. Yao, and X. Wang, "On the power leakage problem in beamspace MIMO systems with lens antenna array," in *Proc. IEEE 86th Veh. Technol. Conf. (VTC-Fall)*, Toronto, ON, Canada, Sep. 2017, pp. 1–5.

[20] S. Lutz and T. Walter, "Lens based 77 GHz TDM MIMO radar sensor for angular estimation in multitarget environments," in *Proc. Eur. Radar Conf.*, Nuremberg, Germany, Oct. 2013, pp. 212–215.

[21] S. Lutz, K. Baur, and T. Walter, "77 GHz lens-based multistatic MIMO radar with colocated antennas for automotive applications," in *Proc. IEEE/MTT-S Int. Microw. Symp. Dig.*, Montreal, QC, Canada, Jun. 2012, pp. 1–3.

[22] V. Pacheco-Peña *et al.*, "Mechanical 144 GHz beam steering with all-metallic epsilon-near-zero lens antenna," *Appl. Phys. Lett.*, vol. 105, no. 24, Dec. 2014, Art. no. 243503.

[23] M. Imbert, A. Papió, F. D. Flaviis, L. Jofre, and J. Romeu, "Design and performance evaluation of a dielectric flat lens antenna for millimeter-wave applications," *IEEE Antennas Wireless Propag. Lett.*, vol. 14, pp. 342–345, 2015.
[24] V. Popov, S. N. Burokur, and F. Boust, "Conformal sparse metasurfaces for wavefront manipulation," Jan. 2020. [Online]. Available: arXiv:2001.09878.
[25] Z.-B. Wang, H. Wu, J.-C. Chen, Z.-H. Wu, and Y.-J. Feng, "An ultralow-profile lens antenna based on all-dielectric metasurfaces," in *Proc. IEEE 5th Asia–Pac. Conf. Antennas Propag. (APCAP)*, Kaohsiung, Taiwan, Jul. 2016, pp. 367–368.
[26] S. Sudo, T. Ide, Y. Kuwahara, and H. Kamo, "Design of multibeam antenna with the dielectric lens and patch array antenna," in *Proc. IEEE Antennas Propag. Soc. Int. Symp. (APSURSI)*, Orlando, FL, USA, Jul. 2013, pp. 2061–2062.
[27] S. Li, Z. N. Chen, T. Li, F. H. Lin, and X. Yin, "Characterization of metasurface lens antenna for sub-6 GHz dual-polarization full-dimension massive MIMO and multibeam systems," *IEEE Trans. Antennas Propag.*, vol. 68, no. 3, pp. 1366–1377, Mar. 2020.
[28] N. Al-Falahy and O. Y. Alani, "Technologies for 5G networks: Challenges and opportunities," *IT Prof.*, vol. 19, no. 1, pp. 12–20, Jan./Feb. 2017.
[29] T. S. Rappaport *et al.*, "Millimeter wave mobile communications for 5G cellular: It will work!" *IEEE Access*, vol. 1, pp. 335–349, 2013.
[30] J. S. Byrnes, Ed., *Advances in Sensing With Security Applications* (NATO Security through Science Series), vol. 2. Dordrecht, The Netherlands: Springer, 2006.
[31] J. Hasch, E. Topak, R. Schnabel, T. Zwick, R. Weigel, and C. Waldschmidt, "Millimeter-wave technology for automotive radar sensors in the 77 GHz frequency band," *IEEE Trans. Microw. Theory Techn.*, vol. 60, no. 3, pp. 845–860, Mar. 2012.
[32] A. Olk and D. Powell, "Accurate metasurface synthesis incorporating near-field coupling effects," *Phys. Rev. Appl.*, vol. 11, no. 6, Jun. 2019, Art. no. 064007.
[33] A. E. Olk, P. E. M. Macchi, and D. A. Powell, "High-efficiency refracting millimeter-wave metasurfaces," *IEEE Trans. Antennas Propag.*, early access, Feb. 28, 2020, doi: 10.1109/TAP.2020.2975840.
[34] G. Gold and K. Helmreich, "A physical surface roughness model and its applications," *IEEE Trans. Microw. Theory Techn.*, vol. 65, no. 10, pp. 3720–3732, Oct. 2017.
[35] S. Yu, H. Liu, and L. Li, "Design of near-field focused metasurface for high-efficient wireless power transfer with multifocus characteristics," *IEEE Trans. Ind. Electron.*, vol. 66, no. 5, pp. 3993–4002, May 2019.
[36] Y. Zárate, I. V. Shadrivov, and D. A. Powell, "Tunable focusing by a flexible metasurface," *Photon. Nanostruct. Fundam. Appl.*, vol. 26, pp. 62–68, Sep. 2017.
[37] G. Lavigne, K. Achouri, V. S. Asadchy, S. A. Tretyakov, and C. Caloz, "Susceptibility derivation and experimental demonstration of refracting metasurfaces without spurious diffraction," *IEEE Trans. Antennas Propag.*, vol. 66, no. 3, pp. 1321–1330, Mar. 2018.
[38] *CST Microwave Studio*, CST, Darmstadt, Germany, 2018.
[39] C. Pfeiffer and A. Grbic, "Metamaterial Huygens' surfaces: Tailoring wave fronts with reflectionless sheets," *Phys. Rev. Lett.*, vol. 110, no. 19, May 2013, Art. no. 197401.
[40] X. Wan, S. L. Jia, T. J. Cui, and Y. J. Zhao, "Independent modulations of the transmission amplitudes and phases by using Huygens metasurfaces," *Sci. Rep.*, vol. 6, May 2016, Art. no. 25639.
[41] J. P. S. Wong, M. Selvanayagam, and G. V. Eleftheriades, "Design of unit cells and demonstration of methods for synthesizing Huygens metasurfaces," *Photon. Nanostruct. Fundam. Appl.*, vol. 12, no. 4, pp. 360–375, Aug. 2014.
[42] B. Yang, T. Liu, H. Guo, S. Xiao, and L. Zhou, "High-performance meta-devices based on multilayer meta-atoms: Interplay between the number of layers and phase coverage," *Sci. Bull.*, vol. 64, no. 12, pp. 823–835, Jun. 2019.
[43] A. A. Fathnan, A. E. Olk, and D. A. Powell, "Broadband anomalous reflection with dispersion controlled metasurfaces," Dec. 2019. [Online]. Available: arXiv:1912.03936.
[44] A. Epstein and G. V. Eleftheriades, "Arbitrary power-conserving field transformations with passive lossless omega-type bianisotropic metasurfaces," *IEEE Trans. Antennas Propag.*, vol. 64, no. 9, pp. 3880–3895, Sep. 2016.
[45] B. L. Good, D. A. Roper, S. Simmons, and M. S. Mirotznik, "Design and fabrication of microwave flat lenses using a novel dry powder dot deposition system," *Smart Mater. Struct.*, vol. 24, no. 11, Oct. 2015, Art. no. 115017. [Online]. Available: https://doi.org/10.1088%2F0964-1726%2F24%2F11%2F115017
[46] X. Ding *et al.*, "Ultrathin pancharatnam–berry metasurface with maximal cross-polarization efficiency," *Adv. Mater.*, vol. 27, no. 7, pp. 1195–1200, 2015. [Online]. Available: https://onlinelibrary.wiley.com/doi/abs/10.1002/adma.201405047
[47] M. A. A. Fathnan and D. D. Powell, "Efficiency calculation of non-periodic metasurface based on modified near field to far field transformation," in *Proc. Asia–Pac. Microw. Conf.*, Kyoto, Japan, 2018, p. 3.
[48] A. Taflove and S. C. Hagness, *Computational Electrodynamics*, 3rd ed. Boston, MA, USA: Artech House, 2005.
[49] A. Olk, K. B. Khadhra, and T. Spielmann, "Highly accurate fully-polarimetric radar cross section facility for mono- and bistatic measurements at W-band frequencies," in *Proc. Antenna Meas. Techn. Assoc. Symp. (AMTA)*, Atlanta, GA, USA, Oct. 2017, pp. 1–6.
[50] R. J. Mailloux, *Phased Array Antenna Handbook* (Artech House Antennas and Propagation Library), 2nd ed. Boston, MA, USA: Artech House, 2005.
[51] J. D. Jackson, *Classical Electrodynamics*, 3rd ed. New Delhi, India: Wiley, 2016.

ANDREAS E. OLK received the B.Sc. and M.Sc. degrees in physics from RWTH University, Aachen, Germany, in 2012 and 2014, respectively. He is currently pursuing the Ph.D. degree in electrical engineering with the University of New South Wales, Canberra, ACT, Australia. Since 2015, he has been affiliated with IEE S.A., Luxembourg. His current research interests include metamaterials, millimeter-wave technology, radar, and automotive sensing.

DAVID A. POWELL (Senior Member, IEEE) received the bachelor's degree in computer science and engineering from Monash University, Melbourne, VIC, Australia, in 2001, and the Ph.D. degree in electronic and communications engineering from RMIT University, Melbourne, in 2006. He is a Senior Lecturer with the School of Engineering and Information Technology, University of New South Wales, Canberra, ACT, Australia. His research on metamaterials has covered the microwave, millimeter-wave, terahertz, and near-infrared wavelength ranges, in addition to work on acoustic metamaterials. From 2006 to 2017, he was a Researcher with the Nonlinear Physics Centre, Australian National University.